

See discussions, stats, and author profiles for this publication at: <https://www.researchgate.net/publication/260413035>

# ChemInform Abstract: Hollow and Solid Metallic Nanoparticles in Sensing and in Nanocatalysis

ARTICLE in CHEMINFORM · MARCH 2014

Impact Factor: 0.74 · DOI: 10.1002/chin.201409229

---

CITATIONS

23

---

READS

109

3 AUTHORS, INCLUDING:



**Mahmoud A. Mahmoud**

Georgia Institute of Technology

76 PUBLICATIONS 1,808 CITATIONS

SEE PROFILE



**Mostafa A El-Sayed**

Georgia Institute of Technology

676 PUBLICATIONS 55,404 CITATIONS

SEE PROFILE

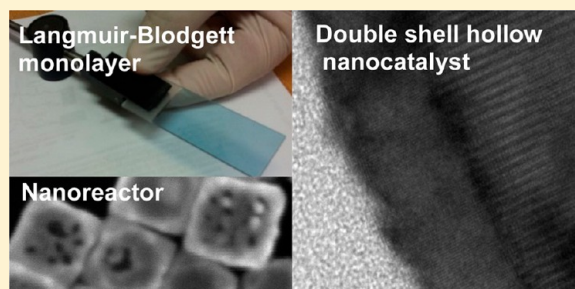
# Hollow and Solid Metallic Nanoparticles in Sensing and in Nanocatalysis

Mahmoud A. Mahmoud, Daniel O'Neil, and Mostafa A. El-Sayed\*

Laser Dynamics Laboratory, School of Chemistry and Biochemistry, Georgia Institute of Technology, Atlanta, Georgia 30332-0400, United States

**ABSTRACT:** When the size of a material is reduced to the nanoscale, at or below the characteristic length scale that determines their properties, the material acquires completely new properties. On this length, its characteristics become sensitive to further changes in size, shape, or whether they are hollow or solid. In this perspective article, we first discuss the different experimental techniques used in the synthesis, assembly, and handling of colloidal solid or hollow nanoparticles with single and double shells. This is then followed by comparing the experimental and theoretical (DDA and FDTD) results for solid and hollow plasmonic nanoparticles as sensors using two different methods. The first method compares the plasmonic enhancement of the radiative properties of molecules or materials (e.g., in surface enhanced Raman scattering, SERS). The second one is based on the amount of the plasmon peak wavelength shift of the nanoparticle in media with different dielectric functions. In the last section of the perspective, we present a summary of the difference between the solid and hollow nanoparticles in nanocatalysis. We present the results of a number of experiments showing that the superior catalytic properties of hollow nanoparticles are due to catalysis occurring within the cavity of the hollow nanoparticles. Finally, using a femtosecond optical technique, we show that adding a second shell of a stiff metal (like Pt or Pd) to the plasmonic hollow nanoparticles increases their mechanical stability.

**KEYWORDS:** hollow nanoparticles, Plasmon field, nanocatalysis, nanoreactor, SERS, substrate effect, sensing, assembling



## I. INTRODUCTION

Metallic nanoparticles have attracted attention because of their excellent optical,<sup>1–3</sup> catalytic,<sup>4</sup> and photothermal<sup>2,5–9</sup> properties which have led to their exciting applications in such fields such as nanocatalysis,<sup>10</sup> nanosensing,<sup>11–14</sup> optical switching,<sup>15,16</sup> magneto-plasmonic devices,<sup>17,18</sup> drug delivery,<sup>19,20</sup> and cancer diagnosis and treatment.<sup>21–23</sup> Many of the photonic and photothermal properties of plasmonic nanoparticles (primarily those of silver and gold) are derived from the strong plasmonic electromagnetic fields resulting from localized surface plasmon resonance (LSPR). LSPR is the coherent oscillation of the collective excitation of the nanoparticle's electrons in the conduction band when excited by light of resonant frequency. This induces very strong surface electromagnetic fields which are stronger than those of the exciting resonant light. Plasmonic nanoparticles can thus enhance the rates of linear optical processes like absorption, fluorescence, and Rayleigh or Raman processes as well as nonlinear processes like second harmonic generation (SESHG),<sup>24</sup> sum frequency generation (SFG) vibrational spectroscopy,<sup>25</sup> and surface enhanced fluorescence.<sup>26</sup> As has been observed for 40 years, plasmon fields can enhance Raman signals by up to  $10^6$  by the process of surface-enhanced Raman spectroscopy (SERS). The combined plasmon fields in-between the assembled plasmonic nanoparticles are very high (hot spots) due to the coupling between the electromagnetic fields resulting from the LSPR of

the conduction band electrons of the individual nanoparticles in the aggregates. If the analyte molecule is located in this region the Raman scattered light can be enhanced by a factor as large as  $10^{14}$ .<sup>27</sup> Fluorescence can also be enhanced as long as the distance or energy level overlap minimizes electron transfer quenching processes of the fluorophore.<sup>28</sup> Rayleigh scattering, as used in dark-field imaging for medical diagnosis and surface imaging, is also enhanced by the plasmonic field of the silver and gold nanoparticles.<sup>21</sup>

The plasmon field also enhances the rates of nonradiative processes such as (1) the nonradiative electronic relaxation in semiconductor-plasmonic metallic nanoparticles,<sup>29</sup> (2) the nonradiative exciton–exciton annihilation processes in conjugated polymers on silver nanocubes (AgNCs) (this can be observed even with the relatively low intensity of a mercury lamp<sup>30</sup>), and (3) the rate of nonradiative retinal photoisomerization,<sup>31</sup> the proton pump process,<sup>33</sup> and the proton photocurrent produced from the photocycle of the photosynthetic system of bacteriorhodopsin.<sup>32</sup>

**Special Issue:** Celebrating Twenty-Five Years of Chemistry of Materials

**Received:** June 27, 2013

**Revised:** August 31, 2013

**Published:** September 3, 2013



There are two main requirements that need to be optimized for the nanoparticle shape for various optical enhancement applications: (1) tuning the LSPR peak in the visible and NIR regions to the optical absorption one needs to enhance and (2) maximizing the plasmonic field strength and distribution<sup>4,33–36</sup> of the selected nanoparticle used for the plasmonic enhancement. Using symmetrical shapes such as spheres,<sup>4</sup> cubes,<sup>35</sup> triangles,<sup>37</sup> shells,<sup>38</sup> hollow nanospheres,<sup>39</sup> nanocages,<sup>35</sup> and frames<sup>40</sup> or asymmetrical shapes such as rods,<sup>34</sup> wires,<sup>41,42</sup> and stars,<sup>43</sup> one is able to enhance the radiative process in the visible and NIR regions of the spectrum. Gold nanorods (AuNRs)<sup>34</sup> and gold nanocages (AuNCs)<sup>35</sup> are particularly useful because they provide LSPR tunability and a strongly enhanced field over a wide range of wavelengths. The LSPRs of AuNRs are tuned by changing the ratio of length to diameter (aspect ratio) while the resonances of AuNCs red shift by decreasing the thickness of the wall without changing the outer size. Moreover, AuNCs are characterized by the presence of distinct plasmon fields on their interior and exterior surfaces.<sup>44</sup> The plasmon field of AuNRs is strongest around their tips.<sup>45</sup> Since the structure of hollow nanoparticles is unique, they must be prepared by special techniques such as template mediation,<sup>46</sup> the Kirkendall effect,<sup>47</sup> or the galvanic replacement<sup>35</sup> techniques.

The catalytic properties of metallic solid nanoparticles stem from their high surface to volume ratio and the presence of a large number of kinetically active atoms on the edges, corners, or defects on the surface of the nanoparticles.<sup>48</sup> This effect is further enhanced with hollow or porous particles like single shell metallic<sup>49–51</sup> and double shell bimetallic nanocatalysts<sup>50,52–56</sup> or supported inside a porous substrate such as a metal–organic framework (MOF),<sup>57</sup> hollow polymer nanofibers,<sup>58</sup> or silica shell coatings of a yolk structure.<sup>59</sup> The enhancement is likely to be due to the confinement cage effect.

Although the small size of nanoparticles is responsible for their exciting properties, this small size also makes their use in many applications difficult. For instance, in plasmon sensing the distance between the plasmonic nanoparticles should be fixed. Additionally, small colloidal nanocatalysts can be difficult to separate from products. Fixing nanoparticles to surfaces can help to minimize these issues and increase the practical use of nanoparticles.

This Perspective focuses on reviewing and discussing: (1) methods used in the synthesis, assembly, and handling of colloidal nanoparticles and (2) the use of plasmonic nanoparticles in sensing applications by enhancing the Raman spectra of attached analytes through the shift in the wavelength of plasmon band by the dielectric function of the added analyte. For both, experimental and computational methods are used. A comparison between solid and hollow nanoparticles is always kept in focus. The last section summarizes the important differences between catalysis by solid and hollow metallic nanoparticles. We recently published an invited article in *Accounts of Chemical Research* summarizing work in the field of nanocatalysis. It emphasized the difference between catalysis with solid nanoparticle and those with hollow nanoparticles. Efficient catalysis with solid nanoparticles occurs on active atoms which are present on corners, edges, and sharp sites present on defect sites while efficient catalysis with hollow nanoparticles occurs on the surfaces of their cavities.<sup>60</sup>

## II. SYNTHESIS AND ASSEMBLY OF COLLOIDAL NANOPARTICLES

### II.A. Synthesis of Solid and Hollow Nanoparticles.

Metallic nanoparticles have been prepared with different shapes, sizes, and compositions by seedless<sup>61</sup> and seed-mediated<sup>62</sup> approaches. In both techniques a small cluster seed is formed which is allowed to grow inside the seed solution (seedless) or is moved to another solution (seed-mediated). During the synthesis, capping agents are used to control (1) the size of the nanoparticle by controlling the rate of capping to stop the nanoparticle growth and (2) the final shape of the nanoparticle obtained depending on the difference between the rates of capping and the thermodynamic stability of the different facets.

Most of metallic nanoparticles are grown from face-centered cubic seed crystals with {111}, {110}, and {100} facets. The symmetrical shapes such as spheres,<sup>4</sup> cubes,<sup>35</sup> octahedral, and prisms,<sup>33,63</sup> result from growth of the {100} and {111} facets while the asymmetric shapes such as rods<sup>34</sup> and wires<sup>41,42</sup> are formed when there is the additional possibility of transfer between the {111} and the high energy {110} facets.<sup>64</sup> The asymmetric shapes can be obtained by symmetry breaking during the growth stage. Physical,<sup>65,66</sup> chemical,<sup>67</sup> and optical<sup>42</sup> techniques have been utilized to change the symmetry of the growing nanocrystals. (1) The physical technique for the symmetry breaking of the nanocrystals growth is based on the variation of the crystallization kinetics and the thermodynamic stability of the growth facets of the nanocrystals. These physical effects were stimulated by varying the concentration of the silver precursor and the capping material used. Both the absolute and relative concentrations of the reactants affect the final shape. At high concentrations, a ratio of polyvinylpyrrolidone capping agent to silver ions of 1.5 produces cubes. At lower concentrations, the same ratio produces nanowires.<sup>35</sup> At ratios above 5, the same reaction will yield quasi-spherical shaped silver nanospheres.<sup>65</sup> Manipulation of reduction kinetics during the growth of the nanocrystals is also another physical technique to break the symmetry of the growth of the nanocrystals.<sup>66</sup> (2) The growth symmetry is broken by using a chemical method such as by the addition of chloride ions or oxygen to etch defect sites on the seeds and drive the crystal growth to form single crystalline nanoparticles.<sup>67</sup> (3) Pentatwinned seeds are obtained during the synthesis of silver nanorods by breaking of the growth symmetry of the silver nanocrystals with light.<sup>42</sup> Recently, we demonstrated a novel mechanical method (high stirring speed) approach for breaking the growth symmetry of silver nanocrystals.<sup>14</sup>

Although the above synthetic technique works for the synthesis of solid metallic nanostructures, hollow nanoparticles (which have cavities and pores in their walls) cannot be prepared using these approaches since growth from a seed necessarily produces a solid structure. Three alternative techniques are used to prepare hollow nanoparticles. The first method is the template-mediated method which was introduced by Mohwald and his group.<sup>46</sup> This technique involves depositing the metal atoms on the surface of a template made of polymer or silica beads. The template is then etched away by H<sub>2</sub>O<sub>2</sub> and HCl. The post-treatment requirement and the roughness of the prepared nanoparticle surfaces limit the usefulness of this technique.

The second method is based on the common metallurgical Kirkendall effect which involves nonequilibrium mutual

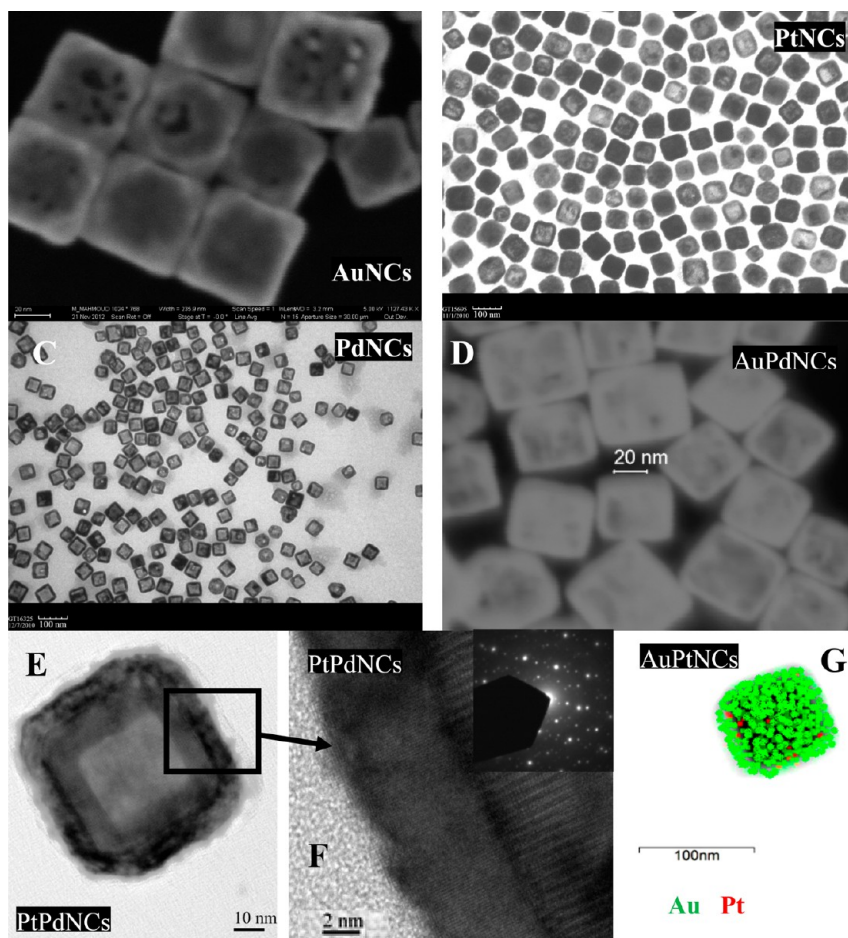


**Figure 1.** (A) SEM image of gold nanocages. (B) TEM of platinum nanocages. (C) TEM image of palladium nanocages. (D) SEM image of gold–palladium double shell nanocages. (E) Magnified TEM image of platinum–palladium double shell nanocages. (F) High-resolution TEM image of platinum–palladium nanocages; the inset is the diffraction pattern for the platinum–palladium nanocages. (G) EDX-SEM mapping of gold–platinum double shells hollow nanoparticles.

diffusion of counter atoms through a reaction interface.<sup>47,68</sup> Since the diffusion flow rates and sizes of the elements are not similar, an internal vacancy is formed inside the nanoparticle. This technique is limited to the synthesis of composite hollow nanoparticles. The most versatile technique for the synthesis of hollow nanoparticles however is the galvanic replacement approach.<sup>35</sup> This technique is based on the galvanic oxidation of two or more atoms in a template nanoparticle by one ion of other metal in solution. The newly reduced metal atoms deposit on the nanoparticle surface. If multiple template atoms are oxidized and dissolve into solution for each deposited metal on the surface, a cavity will be produced. These processes maintain the shape and the size of the nanoparticle while inducing a cavity in its center.

AuNCs (gold nanocages) were the first hollow nanoparticle prepared by this technique and used AgNCs (silver nanocubes) as the template.<sup>35</sup> When gold ions are mixed with a hot solution of AgNCs, three atoms in the AgNCs are oxidized by one gold ion in solution which deposits on the outer surface of the template. Figure 1A shows the SEM image of AuNCs prepared by galvanic replacement. The AuNCs are empty inside and have pores on their Au surfaces.

We modified the galvanic replacement technique to prepare transition metal nanocages of Pt and Pd with superior qualities. By carrying out the galvanic replacement at room temperature and controlling the rate of addition of salt to the template

solution we have produced hollow nanoparticles with catalytic potential.<sup>50</sup> The TEM images of PtNCs and PdNCs prepared by the modified galvanic replacement technique are shown in Figure 1B,C.

We have extended the galvanic replacement technique to double shell hollow nanoparticles. We have prepared bimetallic, hollow nanoparticles with a variety of plasmonic and non-plasmonic metals including gold–platinum (AuPtNCs), gold–palladium (AuPdNCs), platinum–palladium (PtPdNCs), and palladium–platinum (PdPtNCs).<sup>50,51</sup> Figure 1D shows an SEM image of AuPdNCs. The outer surface of the hollow nanoparticles is smooth while the walls of the nanocages contain pores. In order to analyze the composition of the double shell hollow nanoparticles accurately, HR-TEM and EDX-SEM mapping are used. Figure 1E shows the TEM image of a single PtPdNC. The nanoparticles appear to have two shells. The HR-TEM imaging of the wall shows three layers: an outer layer of pure platinum, a pure palladium inner layer, and an alloy layer in between. The inset image of Figure 1F shows a diffraction pattern which corresponds to the two metals. The second imaging technique, EDX-SEM mapping, provides elemental analysis of the outer metal of the cage. Figure 1G shows the EDX-SEM elemental mapping of AuPtNCs revealing that the outer surface is pure gold.

**II.B. Assembling of Nanoparticles on a Substrate.** The applications of nanoparticles are limited by their small size and



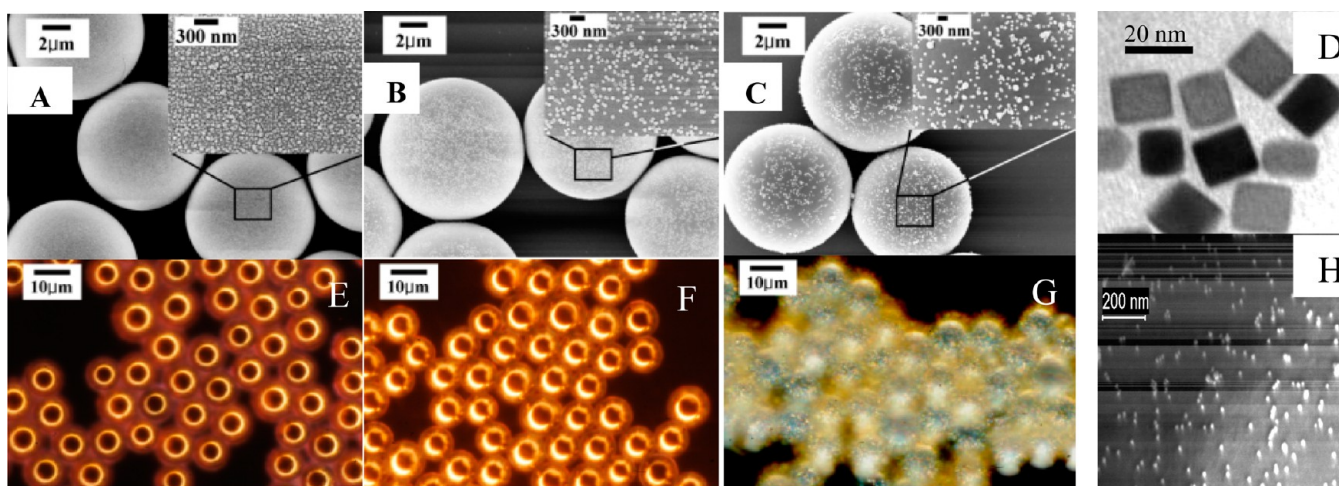


**Figure 2.** SEM images of nanoparticles coating 10  $\mu\text{m}$  polystyrene beads: (A) 30 nm gold nanospheres, (B) 80 nm gold nanospheres, (C) 60 nm silver nanocubes, (H) platinum nanocubes. (D) TEM image of platinum nanocubes. Dark field images of 10  $\mu\text{m}$  PS beads covered by metal NPs: (E) 30 nm AuNPs, (F) 80 nm AuNPs, and (G) 60 nm AgNCs.

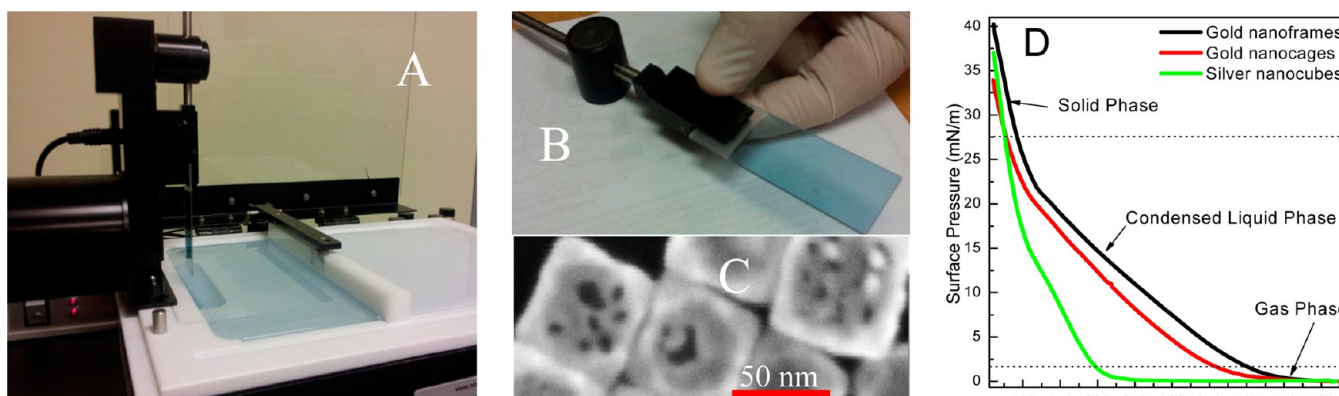


**Figure 3.** (A) Picture of a Langmuir–Blodgett trough after depositing a monolayer of AuNCs on the top of the water sublayer. (B) AuNCs monolayer deposited on the surface of glass slide. (C) SEM image of AuNCs. (D) Langmuir–Blodgett isotherm for AgNCs, AuNCs, and AuNFs measured on the top of water sublayers.

difficulty in handling and recovery. Different methods have been used to overcome the handling problems. For instance, nanoparticles can be fabricated on the surface of a substrate by lithographic techniques such as electron beam (e-beam) lithography<sup>69</sup> and nanosphere (NS) lithography.<sup>70</sup> These techniques involve fabrication of a template followed by deposition of the nanoparticle material and finally removal of the template. For e-beam lithography, an electron beam carves these templates out on a thin polymer film on a substrate. Although this technique succeeded in the fabrication of the nanoparticles on the surface of a substrate, high cost, technical difficulty, limited morphological scope, and the polycrystallinity of the product limit the applicability of this technique.

Nanosphere lithography uses a monolayer of self-assembled microsphere polymer beads on the surface of a substrate. When this template is placed in a gold or silver atom sublimation chamber, the atoms fill in the prismatic voids in between the beads on the substrate. Dissolving the polymer beads leaves a beautiful pattern of gold or silver prisms on the substrate. This technique can only produce prisms but does allow for size control by varying the size of the polymer beads.

Colloidal chemical methods are the most commonly used techniques for synthesizing nanoparticles. Many shapes, sizes,

compositions, and crystal structures have been prepared by these techniques. However, colloidal nanoparticles often have problems with stability and recycling. We suggest two methods to overcome these problems:

(1) *Loading onto Microparticle Supports.* This method involves either the in situ reduction of metal ions on the surface of the support or loading of already synthesized nanoparticles onto the support. Reduction of the metal ions on the support produces different shapes and sizes of nanoparticles, but the loading of already synthesized particles permits the use of the extensive library of colloidal nanoparticle syntheses. Recently, we introduced the solvent-controlled swelling and hetero-coagulation technique<sup>71–73</sup> to load different kinds of nanoparticles onto the surface of a polystyrene (PS) polymer bead support. This method involves swelling the PS by up to 200% using an organic solvent like THF. The resultant pores and channels anchor and trap the capping materials bound to the surface of the nanoparticles. The beads are then washed in a nonswelling solvent which shrinks the beads and fixes the nanoparticles. We were able to use this technique to coat PS with nanoparticles such as 30 and 80 nm polyvinylpyrrolidone (PVP) capped gold nanospheres. Figure 2 A,B shows the SEM images of 10  $\mu\text{m}$  PS beads coated with 30 and 80 nm gold

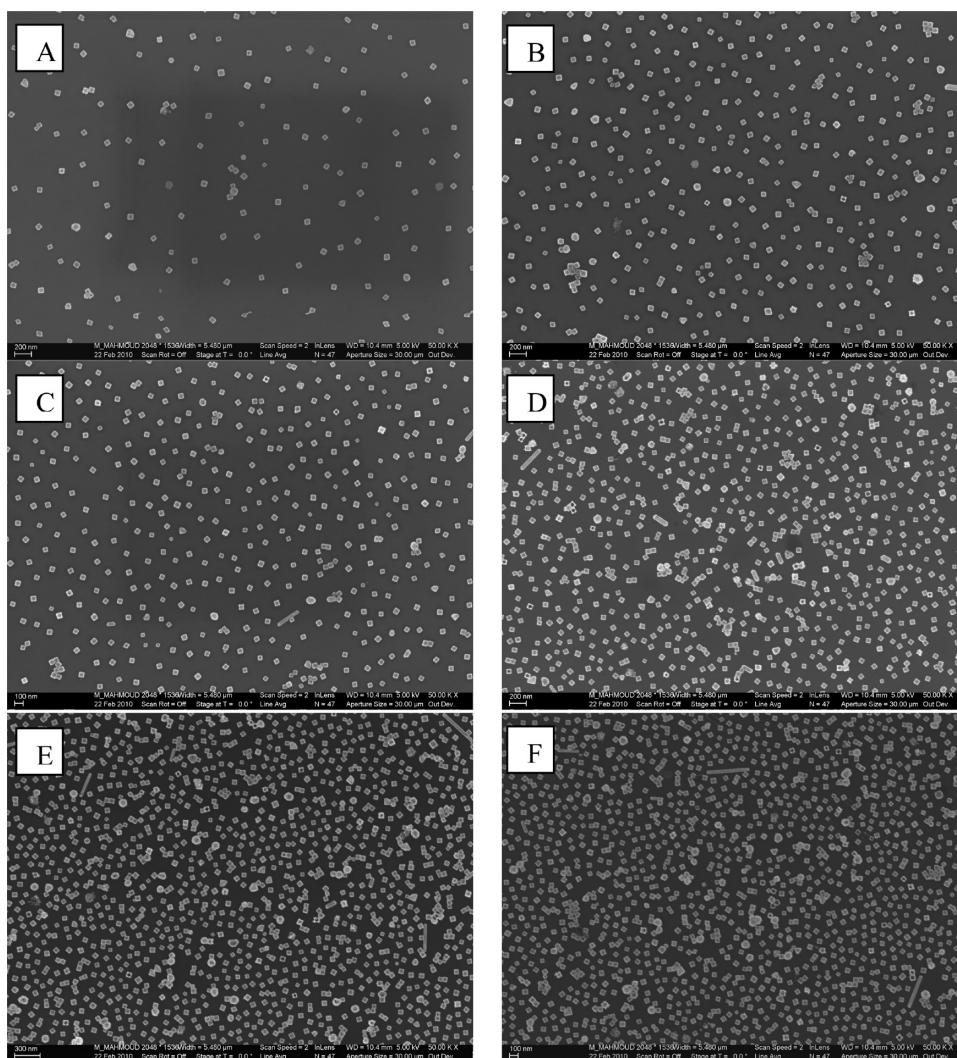


**Figure 4.** A–F: SEM images of AuNC monolayers assembled on the surface of a silicon wafer at surface pressures of 0, 0.5, 1, 2, 4, and 6 mN/m, which correspond to 4, 7, 10, 17, 25, and 29% coverage, respectively.

nanoparticles, respectively. Figure 2 E,F shows the dark field scattering images of PS coated with 30 and 80 nm gold nanospheres, respectively. This technique is applicable to other shapes and materials so long as the capping agent is polymeric or cationic such as trimethyltetradecylammonium bromide (TTAB). Figure 2C (SEM) and 2G (dark field) shows PS coated with silver nanocubes capped with PVP. Figure 2D shows the TEM image of 20 nm platinum nanocubes (top) and SEM image of PS coated with platinum nanocubes capped with TTAB.

(2) *Use of the Langmuir–Blodgett Technique.* The Langmuir–Blodgett technique is useful for assembling monolayers (or multilayers) of colloidal nanoparticles on substrate surfaces. This technique requires that the nanoparticles be dispersed in a volatile solvent, such as chloroform, that is immiscible with the denser sublayer liquid filling the Langmuir–Blodgett trough, such as water. The surface tension of the sublayer liquid forces the added volatile top solvent to form a uniform layer. As the volatile solvent evaporates, the nanoparticles will arrange into a monolayer on the surface of the sublayer as postulated by Langmuir. The interparticle separation distance between the nanoparticles can be controlled by varying the number of particles per trough area. The LB film

can be transferred to a substrate by the dipping method. Figure 3 A shows AuNCs (dispersed in chloroform) sprayed over the surface of the water sublayer of the LB trough. The mechanical barrier is separating the blue colored nanoparticles (left) from the unused water surface (right). The AuNCs are transferred to the surface of a glass slide substrate by dipping it perpendicularly into the solution at the end of the LB trough and slowly pulling it out. Figure 3B shows a glass substrate with a coating of the AuNCs of the SEM image shown in Figure 3C.

The concentration of nanoparticles on the surface affects the surface tension of the water sublayer. Thus, the percent of coverage density can be measured by a Wilhelmy plate attached to a pressure sensor.

The relationship between the surface pressure and the amount of the sublayer area over which the nanoparticles are distributed (the isotherm) indicates how the nanoparticles interact with the sublayer surface and with one another.<sup>74</sup> Figure 3D shows the LB isotherm of AgNCs, AuNCs, and AuNFs. The isotherms exhibit three distinct regions indicating three different modes of interaction between the nanoparticles. These modes bear similarities to the common physical phases and so are termed gaseous, condensed liquid, and solid. In the gaseous state the nanoparticles have a significant average



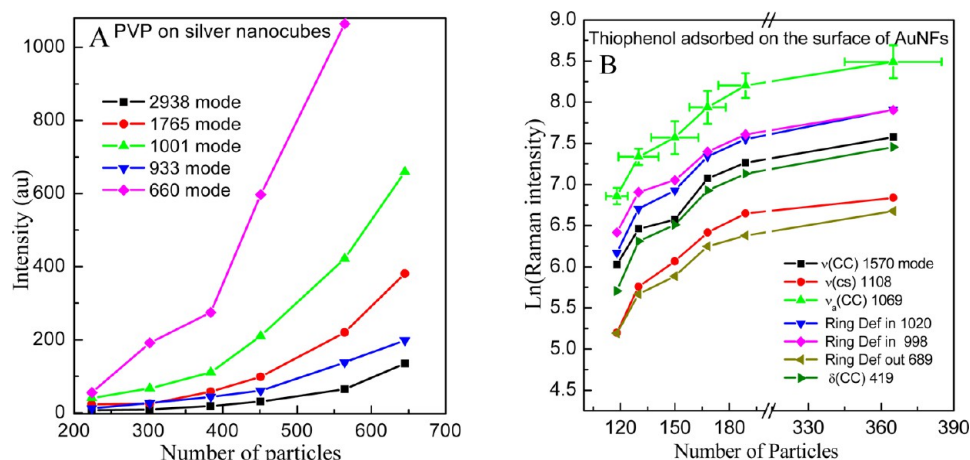


**Figure 5.** Effect of aggregation of solid and hollow nanoparticles on the plasmonic Raman enhancement: (A) PVP capping material coating silver nanocubes (solid nanoparticles) and (B) thiophenol adsorbed on the surface of gold nanoframes (hollow nanoparticles).

separation like gases in a closed container. This phase is highly compressible, and changes in area barely affect the surface pressure. The area at which we observe the gas to liquid phase transition is determined by the relative strengths of the particle–particle and particle–water surface interactions. AuNFs and AuNCs have much weaker interactions with the surface due to their porosity. This makes the interparticle interaction relatively stronger than for the silver nanocubes; thus, the condensed liquid phase sets in earlier for the porous nanoparticles. The slope of the isotherm in the condensed liquid phase depends upon the amount of PVP on the surface of the particles. Eventually, the liquid phase condenses to a solid which consists of a nearly perfectly dense and highly ordered film. The onset area for the solid phase is affected, in part, by the amount of capping material. Since silver nanocubes have higher PVP loading, they will aggregate into the solid phase sooner than the porous gold structures.

Nanoparticles prepared by the colloidal chemical method can be assembled into monolayers at different separation distances by the LB technique. The SEM images of AuNCs assembled into LB monolayers at surface pressures of 0, 0.5, 1, 2, 4, and 6 mN/m are shown in Figure 4 (A–F). Using the Image-J program, the percent of area covered by the AuNCs was calculated to be 4, 7, 10, 17, 25, and 29% for samples prepared at 0, 0.5, 1, 2, 4, and 6 mN/m, respectively. The advantages of the LB technique are the following. (1) It works for nanoparticles of different shapes and sizes. (2) Substrates of different dimensions can be coated with a monolayer (we have successfully coated substrates of up to 10 cm × 10 cm). (3) The amount of nanoparticles per unit area can be controlled (percent of coverage); (4) It is a simple and cost-effective technique.

### III. PLASMONIC NANOSENSING

**III.A. Sensors Based on Plasmonic Surface Enhancement of Raman Scattering (SERS) by Solid or Hollow Nanoparticles.** Plasmonic nanoparticles are capable of enhancing the Raman signal of analyte molecules adsorbed on their surfaces or present within their electromagnetic plasmon field. The enhancement of Raman signal by the plasmonic nanoparticles has been attributed to two mechanisms: the chemical<sup>75</sup> and the electromagnetic.<sup>76</sup> The chemical mechanism of Raman enhancement involves charge transfer

between the chemisorbed analyte and the metallic nanoparticles.<sup>77</sup> This increases the electron density around the analyte which increases its polarizability.<sup>78</sup> The majority of the observed SERS enhancement results are, rather, from the electromagnetic plasmonic mechanism. The surface plasmon resonance supported on the metal surface produces a greatly enhanced electromagnetic field. Thus, the incident laser photon, used during the Raman measurement, and the Raman signal from the analyte get enhanced by this electromagnetic plasmon field which produces greater Raman scattering.<sup>76</sup> The Raman signal can be enhanced up to  $10^6$  on the surface of a single particle and by as large as  $10^{14}$  if the molecule is present in the hot spots of the strong plasmonic field present plasmonic aggregates.<sup>27</sup> It is well-known that the surface plasmon field in between a pair of nanoparticles is much stronger than that of a single nanoparticle due to the strong coupling between the plasmon fields of the two solid neighboring nanoparticles.<sup>27–30</sup> Therefore, nanoparticle aggregates are used for studies using SERS rather than single nanoparticles.<sup>31–33</sup>

Would this large enhancement observed upon the aggregation of solid nanoparticles be detected upon the aggregation of hollow nanoparticles? In order to examine the effect of structure of the nanoparticles (solid and hollow) on the SERS enhancement, AgNCs and AuNFs were studied in a SERS enhancement experiment. The nanoparticles were assembled into monolayers on the surface of a quartz substrate by the Langmuir–Blodgett technique at different coverage densities (thus at different interparticle distances). The Raman spectra of both the PVP capping polymer molecules adsorbed on the surface of AgNCs and of added thiophenol molecules adsorbed on the surface of AuNFs were measured at different nanoparticle coverage densities. Figure 5A shows the relationships between the Raman band intensity of some PVP vibration bands and the number of silver nanocubes exposed to the Raman laser during the measurement. The relationship between the logarithm of the Raman band intensity of thiophenol and the number of AuNFs exposed to the laser beam is shown in Figure 5B. It follows from this figure that nanoparticle aggregation is responsible for Raman enhancement on the solid nanoparticles.<sup>28,34,35</sup> However, as observed, the SERS band intensity of thiophenol adsorbed on the AuNFs monolayer increases more slowly with increasing aggregation.<sup>79</sup>

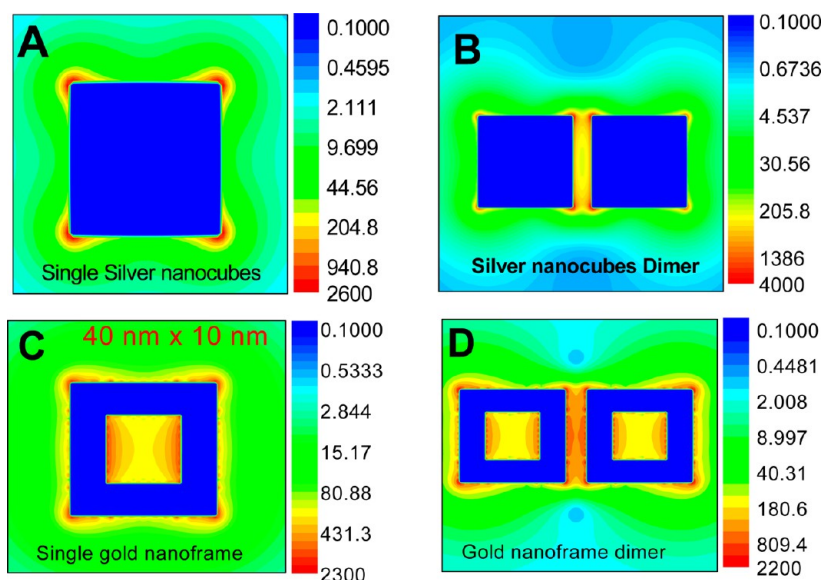


**Figure 6.** Effect on the plasmonic field strength due the coupling between two solid nanocubes (two of A vs B) compared with the coupling between two hollow nanoframes (two of C vs D) (all have similar dimensions). Field distribution calculated by using the DDA technique for (A) individual AgNC, (B) AgNC dimer, (C) single AuNF, and (D) AuNF dimer.

The Raman enhancement by separate solid nanoparticles, such as silver nanocubes, is less efficient than their aggregates. The opposite is observed for hollow nanoparticles such as AuNFs and AuNCs.<sup>44</sup> In order to understand the different SERS behavior of hollow and solid nanoparticles, we calculated, using the discrete dipole approximation (DDA), the plasmon field enhancement of AgNCs and AuNFs alone and as dimers with a small separation distance. The plasmon field enhancement of AgNCs dimers is higher than that of single nanoparticles due to the plasmon field coupling, Figure 4 A,B. This is consistent with what has been reported for all solid nanoparticles. The behavior is different for hollow AuNFs (Figure 6 C,D): the plasmon field intensity of the single AuNF is higher than that of its dimer. The reason for this discrepancy is that the hollow AuNFs have plasmon fields inside and outside the frame (as shown in Figure 6).<sup>79</sup> These fields strongly couple and produce a higher overall field in the single AuNF. The effect of the interparticle coupling reduces the strong intraparticle coupling. As a result there is relatively less coupling enhancement in the coupled dimers of the hollow AuNFs.<sup>79</sup>

The differences between the plasmonic properties of the solid and the hollow nanoparticles are as follows: (1) The hollow nanoparticles have two coupled plasmonic fields: inside and outside. (2) The surface area of the hot spots (in-between strongly coupled plasmonic nanoparticles) is larger for the hollow than for the solid ones. (3) The overall plasmonic field intensity of a pair of coupled solid nanoparticles is larger than that for the two uncoupled single nanoparticles (the origin of the hot spots).

**III.B. Sensors Based on the Dependence of the Wavelength of the LSPR on the Dielectric Function of the Medium.** The resonance frequency of the plasmonic nanoparticles depends on the size of the nanoparticle, the frequency dependent dielectric function of the metal, and the dielectric function of the surrounding medium.<sup>45</sup> The shape of the plasmonic nanoparticles also has a great effect on the peak position and number of peaks observed. As the dielectric function of the environment is varied, the LSPR peak will shift

correspondingly. This may be harnessed for qualitative and quantitative sensing since the LSPR shift will depend on the specific relative permittivity and surface coverage of the adsorbed analyte. The nanoparticles cannot recognize the specific analyte present in the surrounding medium but instead sense the overall change of the dielectric constant of the environment (both solvent and analyte(s)). Specificity may be increased by decorating the nanoparticle with analyte specific receptors.

The sensitivity of the plasmonic nanoparticles is quantified by the sensitivity factor (SF). The SF is defined as the shift in the LSPR peak of the nanoparticle per unit in the refractive index of the surrounding medium. The SF has the units of nm/RIU, where RIU is the refractive index unit. A higher SF indicates that a smaller change in the refractive index of the analyte covering the plasmonic nanoparticle induces larger shift of the surface Plasmon band.

We have measured the SF of the hollow gold nanospheres and AuNFs having different dimensions (wall length and wall thickness). We found them to be more sensitive than solid nanoparticles (see Table 1).<sup>80,81</sup> This is undoubtedly due to the stronger plasmonic field on the surface of the hollow nanoparticles as a result of the coupling between the inner and outer surfaces present in the hollow nanoparticles.

From Table 1, it is clear that the sensitivity factors of the hollow nanoparticles are larger than those of solid nanoparticles of similar dimensions. As mentioned in the former section, hollow nanoparticles have stronger plasmonic fields compared with solid nanoparticles.<sup>84</sup> The important question is: what is the effect of the shape and wall thickness of the hollow nanoparticles on their plasmonic field intensity and thus on their sensitivity factors?

In order to examine the effect of wall thickness and wall length on the SF of AuNFs, DDA calculations were carried out for AuNFs of four different wall lengths and four different wall thicknesses for a total of 16 configurations. The calculations yielded the LSPR of each AuNF in 10 different dielectric media. Table 2 shows how the sensitivity factors of AuNFs depend on the ratio the length to the wall thickness ( $L/T$ ) of AuNFs.



**Table 1. Comparison of the Experimentally Determined Sensitivity Factors of Different Plasmonic Nanoparticles Showing that Hollow Nanoparticles Are Much More Sensitive than Solid Ones**

particle shape	nm/RIU
gold nanospheres	44 <sup>80</sup>
gold nanocubes	83 <sup>80</sup>
gold nanorods	150–285 <sup>80</sup>
hexagonal silver array	191 <sup>81</sup>
silver nanocubes	113 ± 5 <sup>82</sup>
hollow gold nanospheres	298 ± 7
hollow gold nanocages	408 <sup>83</sup>
gold nanoframes <sup>84</sup>	51 wall length, 10 nm thickness
	42 wall length, 9 nm thickness
	83 wall length, 19 nm thickness
	35 wall length, 10 nm thickness
	620 ± 15
	516 ± 24
	508 ± 33
	409 ± 6

**Table 2. Dependence of the Sensitivity Factors on the  $L/T$  Aspect Ratio of Nanoframes of Different Sizes As Predicted from DDA**

wall length (nm)	wall length to wall thickness ( $L/T$ ) aspect ratio			
	4.1	4.5	5.0	5.5
40	500	562	643	739
50	499	559	640	731
80	496	542	636	717
90	494	541	628	712

Experimental measurement and theoretical calculation lead to the following conclusions:<sup>84</sup> (1) For AuNFs of a certain size, SF values increase as the wall thickness decreases. (2) The SF value depends greatly on the ratio between the wall length and the wall thickness (aspect ratio), but for AuNFs of the same aspect ratio, the SF value increases as the wall length decreases.

In order to understand the effect of size on the sensitivity factor of AuNFs of constant aspect ratio, the plasmon field of four different AuNFs of the same wall length and same aspect ratio were calculated. Figure 7 shows the plasmon field distribution of AuNFs of aspect ratio of 4.1 and wall length of 40, 50, 80, and 90 nm. The plasmon field intensity increases as the wall length of the nanoparticles decreases. For AuNFs of small wall length, the coupling between the inner surface fields within the nanoparticles becomes possible resulting in a strong overall plasmonic field.

The SF value of hollow gold nanospheres is as high as hollow gold cubes. DDA calculations were carried out to understand the reason for the high SF values of the spherical hollow plasmonic nanoparticles. Is it due to the plasmonic field coupling of the interior and exterior surfaces as in the case of AuNFs?

The plasmonic field intensity of the outer and interior surfaces of hollow gold nanospheres with four holes penetrating their walls was calculated (see Figure 7 E,F). The plasmon field intensity is high on the pores, and thus the reason of the high sensitivity factors of the hollow spheres (AuHNSs) is not the same as for the hollow cubes (AuNCs).<sup>85</sup>

In order to optimize the plasmonic nanosensors the following difficulties have to be overcome: (1) The plasmon fields of the plasmonic nanoparticles have to be strong enough to make the shift in the LSPR peak large enough to be observed. Nanoparticles with higher plasmon fields are better. (2) Since the LSPR peak shift is not analyte specific, the surfaces of the particles have to be coated with receptors to specifically bind the analyte molecule. (3) The nanoparticles have to be fixed on the surface of a substrate at a small distance to allow their plasmon fields to couple to each other but not so close that the analyte cannot reach the surface. If the nanoparticles shift during a measurement, additional errors are introduced. This leads to yet another consideration: does

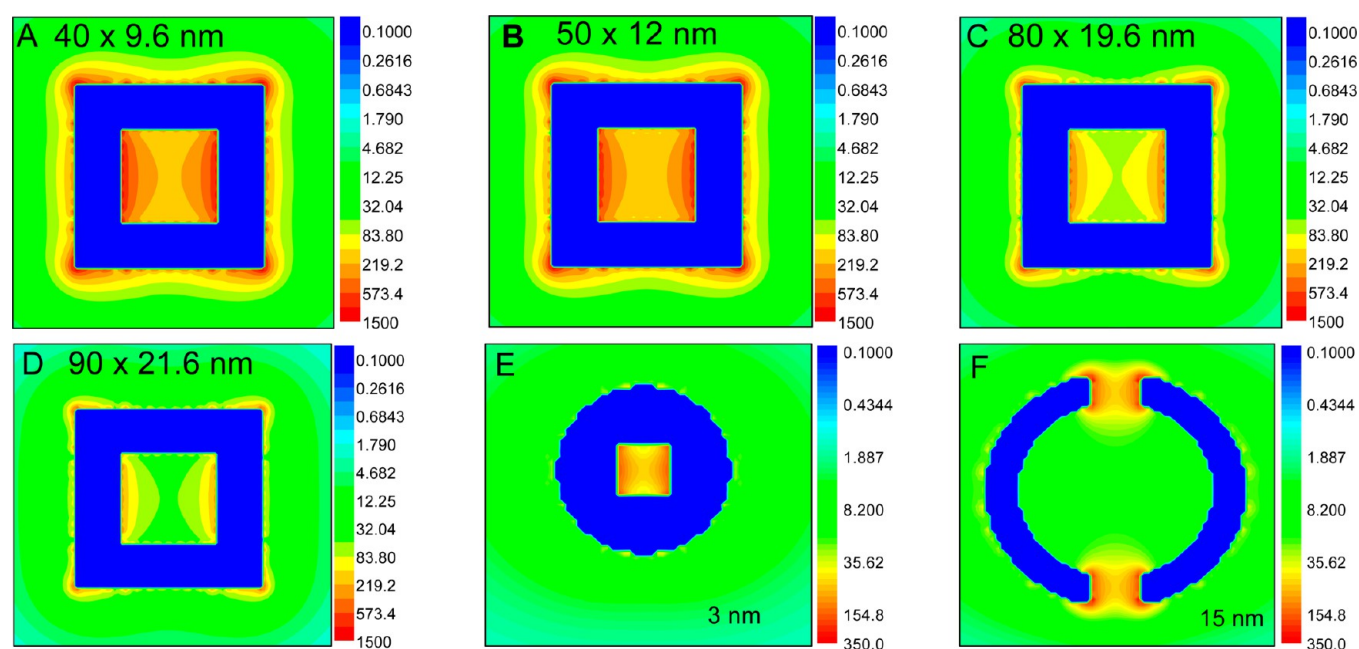


**Figure 7.** Calculated field enhancement map contour of AuNFs of the same aspect ratios ( $L/T = 4.1$ ) with different wall lengths and wall thicknesses. (A) The wall length is 40 nm with a 9.6 nm thickness; (B) wall length is 50 nm with 12 nm thicknesses; (C) wall length is 80 nm with 19.2 nm thicknesses; and (D) wall length is 90 nm with 21.6 nm thickness. The field enhancement map contour of gold hollow spheres: (E) 3 nm from the outer surface, (F) on the middle of the hollow nanoparticle.

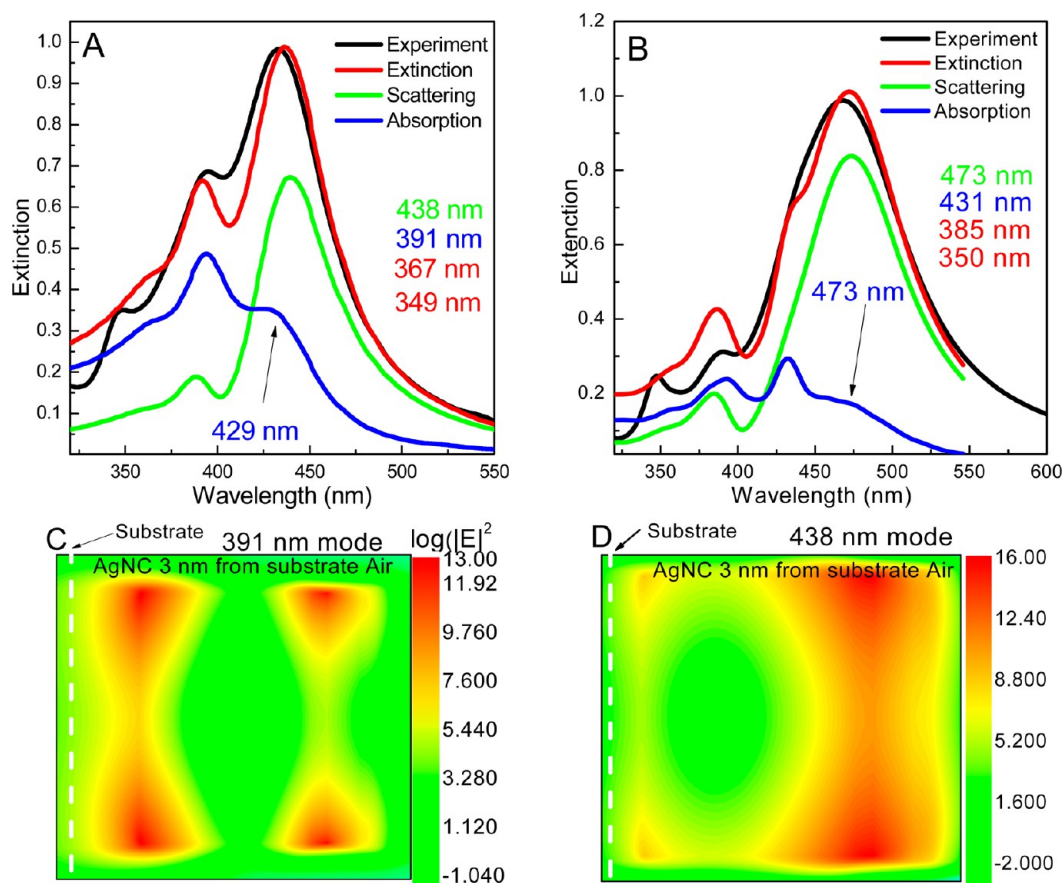


**Figure 8.** Effect of the substrate on the LSPR spectrum (top) and field intensity (bottom): (A) The LSPR spectrum of 65 nm AgNCs (total extinction, scattering, and absorption) calculated with FDTD at a 3 nm separation distance from a quartz substrate. (B) The LSPR spectrum of 65 nm AgNCs (extinction, scattering, and absorption) calculated with FDTD at 2 nm separation distance from a quartz substrate and surrounded with water. The field intensity in log scale ( $\log(|E|^2)$ ) of AgNCs at a 3 nm distances from a quartz substrate calculated with the FDTD technique for (C) 391 nm mode and (D) 438 nm mode.

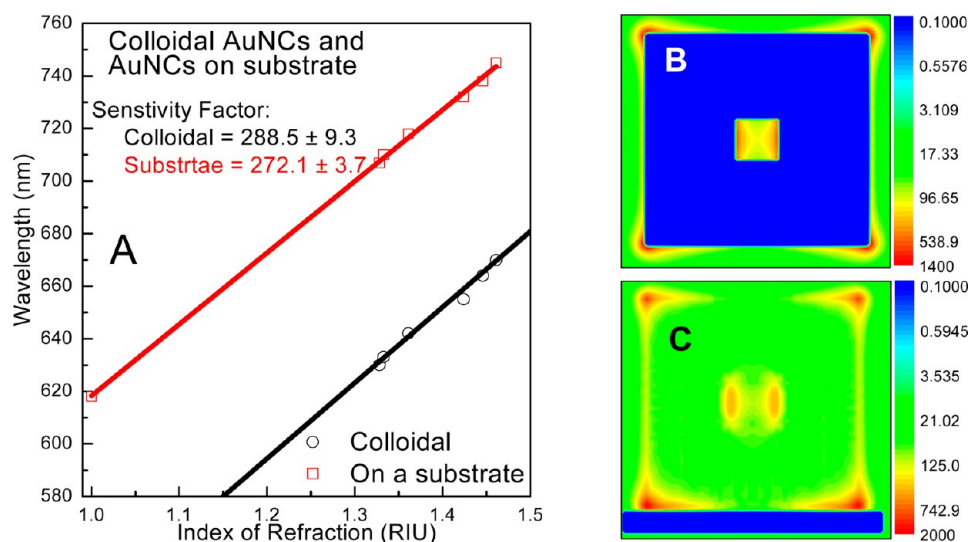


**Figure 9.** (A) Relationship between the LSPR peak maximum of AuNCs measured in different media and the refractive index. The nanoparticles are free in colloidal solution (black) and placed on the surface of quartz substrate (red) in colloidal solution. Plasmon field distribution contours of AuNC calculated by DDA simulation. (B) Field distribution on the outer surface around the hole of colloidal AuNC. (C) Parallel field distribution on the outer surface around the hole of AuNC placed on the surface of the quartz substrate.

the substrate affect the sensing efficiency of the nanoparticles and does the FWHM of the LSPR of the nanoparticles change during sensing?

**III.C. Effect of Substrate on the Plasmonic Field Distribution and Sensing.** As mentioned earlier, the plasmonic nanoparticles used in sensing should be assembled

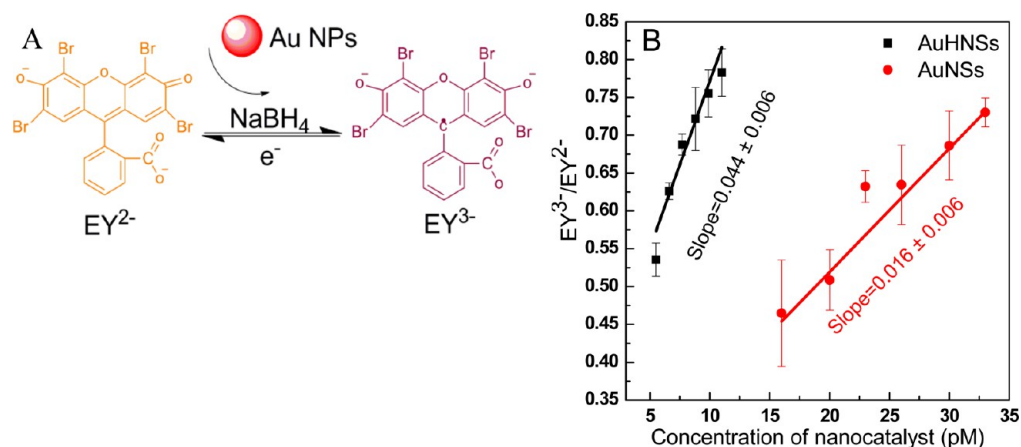


**Figure 10.** Comparison of the catalytic one electron reduction efficiency of the hollow and the solid nanocatalysts of  $EY^{2-}$  with BH: (B) The dependence of the reduction product yield on the nanocatalyst concentration for the catalysis with hollow spheres (black line) and for the solid nanospheres (red line) of comparable size. The slopes of the straight lines are a measure of the catalysts' efficiency which in the case of hollow nanocatalyst is three times that for the solid nanoparticle.

on the surface of a substrate. The substrate affects the sensing efficiency of the plasmonic nanoparticles by changing the plasmon field.<sup>85</sup> In addition, part of the surface of the plasmonic nanoparticles is covered by the substrate.<sup>86</sup> Figure 8A shows the LSPR spectrum of AgNCs assembled on the surface of a quartz substrate with a large separation distance and the LSPR of AgNCs calculated by the finite-difference time-domain (FDTD) simulation technique. The LSPR extinction spectrum of the plasmonic nanoparticles is the sum of absorption and scattering. The experimental results showed that AgNCs placed on a surface of quartz have four LSPR peaks when measured in air. On the basis of the theoretical calculations,<sup>86</sup> the majority of the peak at 438 nm arises from scattering, while the peak at 391 nm arises from absorption. Absorption and scattering contribute roughly equally to the peaks at 367 and 349 nm.

The plasmon field distribution of a free AgNC has octahedral symmetry (see Figure 6A). Placing the AgNC on a substrate reduces the symmetry to  $C_{4v}$ . Figure 8 C,D shows the plasmon field contours for AgNCs placed on the surface of a quartz substrate calculated for different LSPR modes (391 and 438 nm). The change in the plasmon field affects the sensing properties of the plasmonic nanoparticles.

FDTD calculations were carried out to assign the LSPR scattering and absorption spectra of AgNCs placed on quartz substrates in aqueous medium. Changing the medium from air (Figure 8A) to water (Figure 8B) alters the LSPR spectrum of AgNCs placed on a quartz substrate. The extinction peak shifts from 391 to 431 nm (40 nm changes), and the scattering peak at 438 nm is red-shifted to 473 nm (35 nm change) while becoming much broader. In fact, this broadens the entire spectrum.<sup>84</sup>

The reason, according to quasistatic theory,<sup>87</sup> is that the LSPR absorption peak depends on the imaginary part of the polarizability expression while the LSPR scattering peak depends on both the imaginary and the real parts of the polarizability expression. Therefore when the dielectric of the medium is changed, there will be phase differences in the shift of the LSPR scattering and absorption. This causes band broadening dependent on the solvent's dielectric constant and makes it difficult to determine the LSPR peak shift.

In order to study the effect of the substrate on the plasmon field distribution, LSPR peak position, and the SF of hollow nanoparticles, the SF of AuNCs was measured in both colloidal solution and on the surface of a quartz substrate. Figure 9A shows the relationship between the LSPR peak positions of colloidal AuNCs and AuNCs assembled on the surface of a quartz substrate measured in solvents with different dielectric functions. Although the SF of the AuNCs decreased slightly on the quartz substrate, their LSPR peak position blue shifts by  $\sim 80$  nm for colloidal particles in each solvent compared with that on the substrate. To examine the effect of substrate on the plasmon field distribution of AuNCs, the plasmon field contours of colloidal AuNCs were calculated by DDA on the outer surface of the isolated nanoparticle and on the surface of the substrate. In the absence of the quartz substrate, the plasmon field distribution on the outer surface is uniform, the holes have high field intensity, and the plasmon field around the corners is more intense compared with that on the holes. The plasmon field intensity and distribution of AuNCs placed on the surface of a quartz substrate is distorted as shown in Figure 7C. However, the plasmon field distribution close to the quartz substrate is stronger than the field far from the substrate. Moreover, the plasmon field intensity far from the substrate is higher than the field intensity of colloidal AuNC. Breaking the symmetry of the plasmon field distribution by the quartz substrate increases the field intensity near and far from the substrate. But the field close to the surface of substrate does not sense the change of the dielectric of the medium, and this could cause the observed decrease in the SF value of the nanoparticle on the substrate.

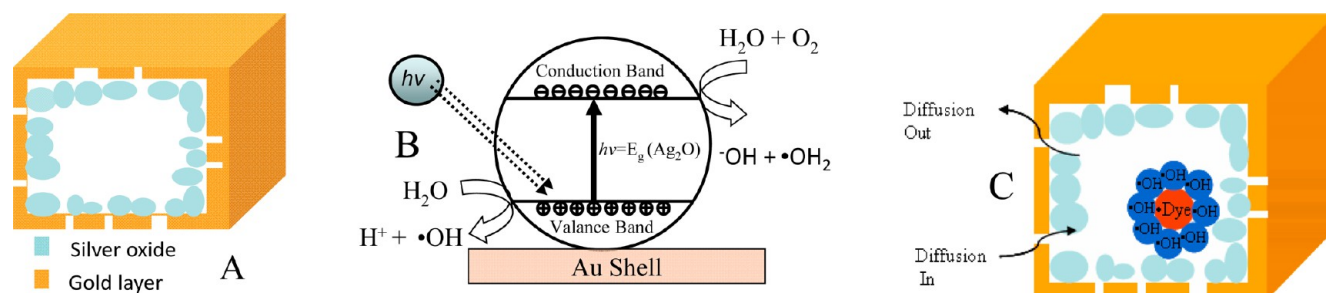
#### IV. NANOCATALYSIS

**IV.A. Summary of the Observations Suggesting that Nanocatalysis with Hollow Nanoparticles Occurs within the Cavities.** The cavities inside hollow nanostructure could provide unique catalytic features which distinguish them from solid nanoparticles. Clearly, a hollow structure provides more surface area. The galvanic replacement technique also produces a rougher and less capped inner surface. Thus, this surface should contain a large number of thermodynamically active atoms which are not covered by the capping agent. Finally, the inner cavity can accumulate reaction intermediates (due to the



**Table 3.** Kinetic Parameters of the Reduction of 4NP with BH Catalyzed by PdNCs, PtPdNCs, PdPtNCs, and PtNCs of Similar Concentrations

nanocatalyst	rate constant at 25 °C ( $\text{min}^{-1}$ )	activation energy (kcal/mol)	entropy of activation (cal/(mol·K))	frequency factor ( $\text{min}^{-1}$ )
PdNCs	$0.0190 \pm 8.7 \times 10^{-4}$	$22.6 \pm 1.5$	$67.8 \pm 5.0$	$5.10 \times 10^{14}$
PtPdNCs	$0.0035 \pm 1.3 \times 10^{-4}$	$20.7 \pm 1.8$	$61.4 \pm 6.0$	$2.13 \times 10^{13}$
PdPtNCs	$0.0190 \pm 2.0 \times 10^{-4}$	$18.5 \pm 1.3$	$50.4 \pm 4.2$	$8.80 \times 10^9$
PtNCs	$0.0036 \pm 2.0 \times 10^{-4}$	$16.2 \pm 1.1$	$43.2 \pm 3.6$	$2.31 \times 10^9$

**Figure 11.** Schematic diagram of (A) AuNC with a layer of silver oxide layer on the inside surfaces of the AuNC, (B) the mechanism of photoformation of the radicals by silver oxide inside the AuNCs nanoreactor, and (C) the reaction and the cage effect inside AuNCs–Ag<sub>2</sub>O nanoreactor.

cage effect) thus enhancing the rate of the reaction if this intermediate is a rate determining species.

The high efficiency of the hollow nanoparticles in catalysis has been reported for a few reactions.<sup>50,51,88</sup> However, it is unclear whether this enhancement is due to the nanoreactor cage effect, the nature of the interior surface, or larger surface area. Experiments have been performed in our laboratory to answer this question and the results can be summarized as follow: (1) Hollow and solid nanospheres of the same outer size were examined and their catalytic activity compared.<sup>89,90</sup> (2) The kinetic parameters of a reaction catalyzed with hollow nanoparticles with double (Pt, Pd) shells of interchangeable order were determined. The results are compared with two single (Pt or Pd) hollow nanoparticles of similar dimensions to each other and to the double shell nanoparticles. The results lead to the conclusion that the kinetic parameters observed for the double shell were those of the interior shell in the two double shell nanoparticles.<sup>50,88</sup> (3) The photocatalytic efficiency of a Ag<sub>2</sub>O catalyst supported on the inside of porous gold was found to be correlated with the number of pores in the hollow nanoparticle and the cavity size. (4) The LSPR spectrum shift during a reaction catalyzed by nanoparticles with plasmonic gold inner and outer surfaces was found to be comparable to that observed when the reaction was catalyzed with a particle that has only an inner plasmonic surface.<sup>51,88</sup>

**IV.B. Catalytic Reduction of the Eosin Dye with Hollow Nanospheres Is More Efficient than with Solid Nanospheres.** Eosin Y dye ( $\text{EY}^{2-}$ ) can be reduced electrochemically by accepting either one or two electrons. Gold nanospheres (AuNSs) and gold hollow nanospheres (AuHNSs) can selectively catalyze the one-electron reduction of  $\text{EY}^{2-}$  with sodium borohydride (BH).<sup>89,90</sup> The reduction pathway of  $\text{EY}^{2-}$  in the presence of the nanocatalysts is shown in Figure 10A. The efficiency of catalysis by the gold nanoparticles was measured by the yield of the one-electron product of  $\text{EY}^{2-}$  reduction. The relationship between the one electron reduction yield and the concentration of the solid and the hollow gold nanospheres is displayed in Figure 10B. The slope of the linear relationship measures the nanocatalyst efficiency. This slope is  $0.044 \pm 0.006$  for the hollow

nanocatalyst but only  $0.016 \pm 0.006$  for the solid AuNSs.<sup>89</sup> This shows that hollow gold spheres are three times more efficient than the solid gold nanospheres of the same size and shape. This might suggest that the catalysis inside the cavity of the hollow catalyst is twice as efficient as the outside surface of either catalyst.

**IV.C. Catalysis with Single and Double Shell Hollow Nanocatalysts.** For any catalysis reaction the kinetic parameters such as activation energy, frequency factor, rate constant, and entropy of activation are constant and depend on the activity of the surface of the catalyst. To show that the inner wall of hollow nanocatalysts is more active (and thus that catalysis occurs on the inner surface), the kinetic parameters were measured for a variety of single and mixed metal catalysts. The kinetic parameters for PtNCs were found to be comparable to PdPtNCs for the reduction of 4-nitrophenol (4NP) with BH. Similarly, the PdNCs and PtPdNCs had comparable values of kinetic parameters for the same reaction. The kinetic parameter values of the reduction of 4NP by BH are summarized in Table 3. The reduction reaction proceeds with a slow rate in the first 5–10 min, and then the rate of the reaction becomes faster. During the first 5–10 min the reaction takes place only on the outer surface with a slow rate as the reactants diffuse into the inner cavity.<sup>50</sup> These results suggest that catalysis by hollow nanocatalysts takes place inside the cavity and that the activity is due to catalysis occurring on the inner surface.

**IV.D. Cage Effect in Catalysis with Hollow Nanostructures.** The photocatalytic degradation of organic dyes such as methyl orange dye (MO) takes place via a free radical mechanism. Semiconductors<sup>89</sup> such as titanium oxide and silver oxide have been used in the photocatalysis of this reaction. When exposed to light, these photocatalysts generate hydroxyl radicals ( $\cdot\text{OH}$ ) from the photochemical reaction with water. The hydroxyl radicals attack the organic dyes and initiate the free radical oxidation reaction.<sup>53</sup> When we used gold nanocages in the catalysis of this reaction, we found that the residual silver inner layer of AuNCs reacts with dissolved oxygen in water to produce the photoreactive silver oxide (Ag<sub>2</sub>O) semiconductor on the inner surface of the cage (Figure 11A). Upon excitation

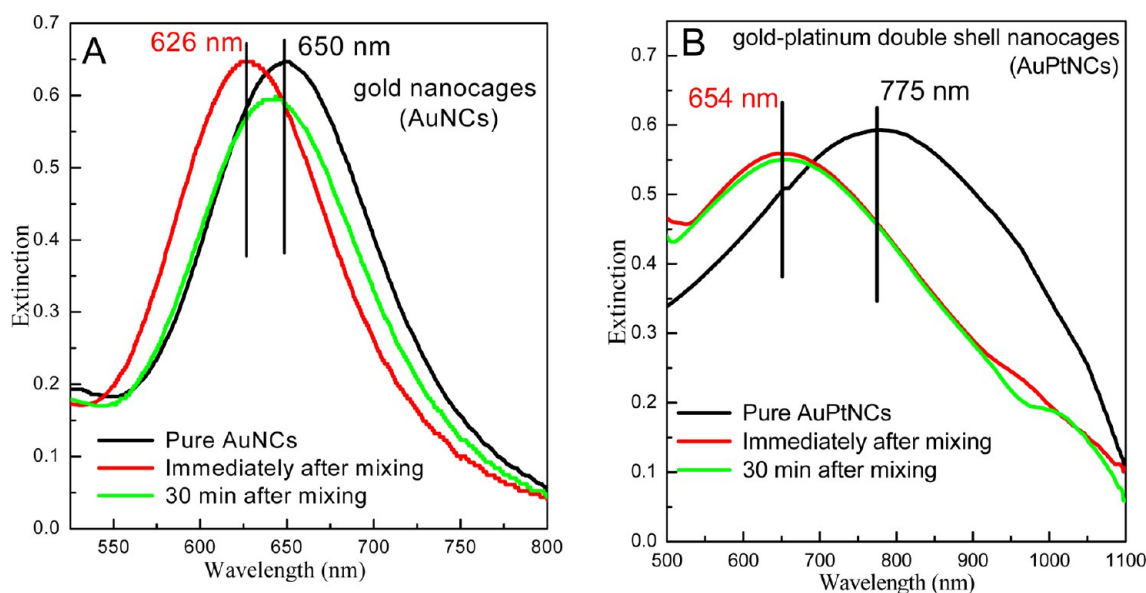


**Figure 12.** Localized surface plasmon resonance spectra of pure nanocatalysts (black), immediately after mixing with borohydride and 4-nitrophenol (red), and 30 min after mixing with borohydride and 4-nitrophenol (green): (A) AuNCs and (B) AuPtNCs.

of AuNCs in water, the silver oxide produces the  $\cdot\text{OH}$  radical as shown in Figure 11B.<sup>53</sup> The  $\cdot\text{OH}$  radicals then attack the MO molecules causing intramolecular fragmentation. This process is summarized in Figure 11C.

AuNCs– $\text{Ag}_2\text{O}$  nanoparticles with different cavity sizes and pore sizes in their walls were examined in the MO photodegradation reaction.<sup>53</sup> The efficiency of this photocatalyst was found to depend on both the number and the size of the pores as well as the cavity size of the nanoparticle itself. Since the  $\text{Ag}_2\text{O}$  catalyst is present only on the inner surface of the AuNCs, the reaction has to occur inside the cage. The reaction rate would thus depend on the steady state concentration of MO concentration inside the cage and the inner surface area covered with the  $\text{Ag}_2\text{O}$ . At a fixed initial MO concentration added, both of these quantities (and the rate of the reaction) are sensitive to the size of the nanoparticle as well as the size and the number of pores on its walls, as observed (see Figure 11C).<sup>53</sup>

**IV.E. Comparing the Shift in the LSPR Spectrum of Hollow Nanocatalysts Containing One Plasmonic Surface with Two Plasmonic Surfaces.** Hollow plasmonic nanoparticles have two plasmonic surfaces (inner and outer). As discussed earlier in the plasmonic sensing section, the LSPR peak shifts when the dielectric constant of the surrounding medium changes.<sup>51</sup> When the dielectric around the inner surface is changed, the LSPR peak shifts, and when the dielectric on the outer surface is changed, further shift in the LSPR peak is expected.<sup>51</sup> This expectation is used to confirm the high catalytic activity of the inner surface of the hollow nanocatalysts.

Two different kinds of plasmonic hollow nanocatalysts were examined. The first had two plasmonic surfaces, such as AuNCs, and the other had one outer plasmonic surface but a nonplasmonic inner surface of Pt (AuPtNCs). Both gold and platinum catalyze the BH reduction of 4NP. This reaction evolves hydrogen gas. During the reaction, the  $\text{H}_2$  gas (refractive index  $\sim 1$ ) replaces water in the aqueous medium (refractive index  $\sim 1.33$ ) around the surface of the nanoparticles. This causes a blue shift in the LSPR peak of the

plasmonic surface. Figure 12 A,B shows the LSPR spectra of AuNCs (two plasmonic surfaces) and AuPtNCs (one plasmonic surface) after mixing with pure 4NP, pure BH, and a mixture of 4NP and BH at 0 and 30 min after mixing, respectively. Two sequential blue shifts in the LSPR of AuNCs are observed. One occurs immediately after mixing and the other after  $\sim 5$  min. In the first 5 min the reaction proceeds slowly but then the rate suddenly increases (as indicated by the second blue shift in LSPR peak) due to the more efficient reaction on the inner surface. A single rapid LSPR blue shift is observed when using a nanoparticle with only one plasmonic surface AuPtNCs hollow nanocatalyst. The reaction begins slowly but, as with the AuNCs, becomes faster after a lag period. This suggests that initially the reaction proceeds via a slow reaction on the outer surface but, after diffusion into the inside cavity, the faster reaction on the inner reaction takes over.

**IV.F. New Optical Technique<sup>91</sup> for Measuring the Mechanical Stability of Hollow Metallic Nanocage Catalysts.** The mechanical stability of nanoparticles is an important factor in determining their practical usefulness for catalysis. Since the materials properties of nanoparticles often differ from the bulk values, it is necessary to do direct measurements on the nanoparticles themselves. The Young's modulus (a measure of elasticity) is a useful and measurable metric for nanoparticle stability.

On the macroscale, the Young's modulus could be determined by making a spring out of the material and observing the frequency with which the spring oscillates—stiffer springs vibrate faster. On the nanoscale we can perform a similar experiment by exciting the electrons in the nanoparticle and measuring the frequency of induced lattice vibrations (phonons). These phonons are typically the breathing mode which consists of the expansion (and later contraction) of the lattice in all directions simultaneously. Since this changes the size of the particle, it will produce a small change in the LSPR peak position.<sup>92,93</sup> By tracking the oscillating extinction at a single wavelength of the LSPR peak over a few hundred

picoseconds after excitation, we can determine the frequency of the lattice vibration.<sup>94,95</sup>

We used this method to determine the effect of adding a second shell of Pt or Pd to plasmonic nanocages. When Pt is placed inside a Au nanoshell the oscillation frequency of the Au is found to increase more than when the interior added shell is made of Pd. This is consistent with the fact that the Young's modulus value (and thus the metallic strength) of bulk polycrystalline Pt is 139 GPa while that of Pd is 115 GPa, compared to only 69 GPa for Au. This optical technique permits the characterization of the basic materials properties of nanoparticles and provides a way to explain and predict how different shapes and sizes of nanocatalysts behave over time.

## V. SUMMARY

The vastly different catalytic and analytical properties of hollow and solid nanoparticles give researchers yet another tunable variable when designing useful nanoparticles. In order to fully characterize these differences it is necessary to have robust techniques for the synthesis and assembly of hollow nanoparticles. To that end we have discussed these techniques and shown how traditional colloidal syntheses for solid nanoparticles may be extended to hollow shapes. We have shown how Langmuir–Blodgett assemblies of hollow nanoparticles differ from solid nanoparticles.

Hollow plasmonic nanoparticles proved to have better sensing properties than solid ones. This is due to (1) the presence of interior and exterior plasmon fields that couple with one another resulting in a much stronger field and (2) the hollow shapes that produce a more evenly distributed plasmonic field. Since hollow nanoparticles exhibit intraparticle coupling of the fields, they are less dependent upon the formation of nanoparticle aggregates to produce a strong signal.

The LSPR extinction spectrum of all plasmonic nanoparticles consists of two parts (absorption and scattering): for sensing by SERS the high scattering is favorable, but for LSPR sensing it has been shown that the absorption and scattering peaks respond to the change of the dielectric function of the surroundings differently. When the dielectric of the environment is changed, the absorption and scattering peaks shift with a different phase which leads to broadening in the LSPR extinction peak. Since SERS relies upon the scattering component, this is not a problem. However, it limits the accuracy of the LSPR sensing method.

Hollow nanoparticles showed better catalytic activity compared with solid nanoparticles. The reason for this is not just that the hollow nanoparticles have greater surface area. Different experimental results suggested that the nanoreactor cage effect and the highly active uncapped and rough inner surfaces also play a large role.

On the basis of the above results we believe that hollow nanoparticles have many features which make them desirable for use in sensing and in catalysis. The question of the mechanical stability of the plasmonic nanocages is discussed, and a new technique was developed for measuring the elasticity of the plasmonic nanocages, whose value is reflected. The results showed that adding another shell of a stiffer metal like Pt or Pd adds more mechanical strength to the nanocages made of the softer gold and silver.

## ■ AUTHOR INFORMATION

### Corresponding Author

\*E-mail: melsayed@gatech.edu.

## Notes

The authors declare no competing financial interest.

## Biographies

Mahmoud A. Mahmoud joined the Laser Dynamics Laboratory, Georgia Tech, in 2007 after receiving his PhD from Cairo University, as a Postdoctoral Associate and later as a Research Scientist II. He received his B.S. degree in chemistry from Zagazig University and M.S. degree in physical chemistry from the National Institute of Laser Enhanced Sciences (NILES) at Cairo University, Egypt, in 2004. Since 2004, he has published over 58 peer-reviewed papers and book chapters.

Daniel O'Neil received a BS in chemistry from Harvey Mudd College where he examined electron transport dynamics in dye sensitized solar cells under the supervision of Professor Hal Van Ryswyk. He is a PhD student of Professor Mostafa El-Sayed at the Georgia Institute of Technology. His current interests center on using ultrafast spectroscopy to track energy transfer in metals and semiconductors.

Mostafa El-Sayed is Julius Brown Chair and Regent Professor in Chemistry at Georgia Tech. His received his Ph.D. from Florida State and was a research associate at Harvard, Yale, and Caltech. He joined UCLA in 1961 and moved to Georgia Tech. in 1994. He was elected member of the U.S. National Academy of Sciences and fellow of the American Academy of Arts and Sciences and received the 2007 USA National Medal of Science in Chemistry in 2008. He and his group have over 600 publications that have received over 50,000 citations and gave him an h-index of over 94.

## ■ ACKNOWLEDGMENTS

The authors would like to acknowledge the financial support of NSF Grant DMR-1206637.

## ■ REFERENCES

- (1) Malinsky, M. D.; Kelly, K. L.; Schatz, G. C.; Van Duyne, R. P. *J. Phys. Chem. B* **2001**, *105*, 2343–2350.
- (2) Kreibitz, U.; Vollmer, M. *Optical Properties of Metal Clusters*; Springer Series in Materials Science 25; Springer: 1995; p 532.
- (3) Tao, A.; Sinsermsuksakul, P.; Yang, P. D. *Angew. Chem., Int. Ed.* **2006**, *45*, 4597–4601.
- (4) Freund, P. L.; Spiro, M. J. *Phys. Chem.* **1985**, *89*, 1074–1077.
- (5) Link, S.; El-Sayed, M. A. *Int. Rev. Phys. Chem.* **2000**, *19*, 409–453.
- (6) Jain, P. K.; Huang, X. H.; El-Sayed, I. H.; El-Sayed, M. A. *Acc. Chem. Res.* **2008**, *41*, 1578–1586.
- (7) Grzelczak, M.; Perez-Juste, J.; Mulvaney, P.; Liz-Marzan, L. M. *Chem. Soc. Rev.* **2008**, *37*, 1783–1791.
- (8) Perez-Juste, J.; Pastoriza-Santos, I.; Liz-Marzan, L. M.; Mulvaney, P. *Gold nanorods: Synthesis, characterization and applications*; Elsevier Science: 2005; pp 1870–1901.
- (9) Huang, X. H.; El-Sayed, I. H.; Qian, W.; El-Sayed, M. A. *J. Am. Chem. Soc.* **2006**, *128*, 2115–2120.
- (10) Freund, P. L.; Spiro, M. J. *Phys. Chem.* **1985**, *89*, 1074–7.
- (11) Jin, R.; Wu, G.; Li, Z.; Mirkin, C. A.; Schatz, G. C. *J. Am. Chem. Soc.* **2003**, *125*, 1643–1654.
- (12) Haes, A. J.; Chang, L.; Klein, W. L.; Van Duyne, R. P. *J. Am. Chem. Soc.* **2005**, *127*, 2264–2271.
- (13) Berger, C. E. H.; Beumer, T. A. M.; Kooyman, R. P. H.; Greve, J. *Anal. Chem.* **1998**, *70*, 703–706.
- (14) Mahmoud, M. A.; El-Sayed, M. A. *J. Phys. Chem. Lett.* **2013**, *4*, 1541–1545.
- (15) MacDonald, K. F.; Samson, Z. L.; Stockman, M. I.; Zheludev, N. I. *Nat. Photonics* **2009**, *3*, 55–58.
- (16) Pohl, M.; Belotelov, V. I.; Akimov, I. A.; Kasture, S.; Vengurlekar, A. S.; Gopal, A. V.; Zvezdin, A. K.; Yakovlev, D. R.; Bayer, M. *Phys. Rev. B* **2012**, *85*, 081401–081406.



- (17) Temnov, V. V.; Armelles, G.; Woggon, U.; Guzatov, D.; Cebollada, A.; Garcia-Martin, A.; Garcia-Martin, J. M.; Thomay, T.; Leitenstorfer, A.; Bratschitsch, R. *Nat. Photonics* **2010**, *4*, 107–111.
- (18) Temnov, V. V. *Nat. Photonics* **2012**, *6*, 728–736.
- (19) Brigger, I.; Dubernet, C.; Couvreur, P. *Adv. Drug Delivery Rev.* **2002**, *54*, 631–51.
- (20) Aymonier, C.; Schlotterbeck, U.; Antonietti, L.; Zacharias, P.; Thomann, R.; Tiller, J. C.; Mecking, S. *Chem. Commun.* **2002**, 3018–3019.
- (21) El-Sayed, I. H.; Huang, X. H.; El-Sayed, M. A. *Nano Lett.* **2005**, *5*, 829–834.
- (22) Loo, C.; Lowery, A.; Halas, N.; West, J.; Drezek, R. *Nano Lett.* **2005**, *5*, 709–711.
- (23) Fortina, P.; Kricka, L. J.; Graves, D. J.; Park, J.; Hyslop, T.; Tam, F.; Halas, N.; Surrey, S.; Waldman, S. A. *Trends Biotechnol.* **2007**, *25*, 145–152.
- (24) Shen, Y. R. *Nature* **1989**, *337*, 519–525.
- (25) Baldelli, S.; Eppler, A. S.; Anderson, E.; Shen, Y. R.; Somorjai, G. A. *J. Chem. Phys.* **2000**, *113*, 5432–5438.
- (26) Aslan, K.; Lakowicz, J. R.; Geddes, C. D. *Curr. Opin. Chem. Biol.* **2005**, *9*, 538–544.
- (27) Michaels, A. M.; Nirmal, M.; Brus, L. E. *J. Am. Chem. Soc.* **1999**, *121*, 9932–9939.
- (28) Lisunova, M.; Mahmoud, M.; Holland, N.; Combs, Z. A.; El-Sayed, M. A.; Tsukruk, V. V. *J. Mater. Chem.* **2012**, *22*, 16745–16753.
- (29) Mahmoud, M. A.; Qian, W.; El-Sayed, M. A. *Nano Lett.* **2011**, *11*, 3285–3289.
- (30) Mahmoud, M. A.; Poncheri, A. J.; Phillips, R. L.; El-Sayed, M. A. *J. Am. Chem. Soc.* **2010**, *132*, 2633–2641.
- (31) Gai, F.; Hasson, K. C.; McDonald, J. C.; Anfinrud, P. A. *Science* **1998**, *279*, 1886–1891.
- (32) Yen, C. W.; Hayden, S. C.; Dreaden, E. C.; Szymanski, P.; El-Sayed, M. A. *Nano Lett.* **2011**, *11*, 3821–3826.
- (33) Jin, R. C.; Cao, Y. W.; Mirkin, C. A.; Kelly, K. L.; Schatz, G. C.; Zheng, J. G. *Science* **2001**, *294*, 1901–1903.
- (34) Jana, N. R.; Gearheart, L.; Murphy, C. J. *J. Phys. Chem. B* **2001**, *105*, 4065–4067.
- (35) Sun, Y. G.; Xia, Y. N. *Science* **2002**, *298*, 2176–2179.
- (36) Nikoobakht, B.; El-Sayed, M. A. *Langmuir* **2001**, *17*, 6368–6374.
- (37) Jin, R.; Cao, Y. C.; Hao, E.; Metraux, G. S.; Schatz, G. C.; Mirkin, C. A. *Nature* **2003**, *425*, 487–490.
- (38) Oldenburg, S. J.; Averitt, R. D.; Westcott, S. L.; Halas, N. J. *Chem. Phys. Lett.* **1998**, *288*, 243–247.
- (39) Schwartzberg, A. M.; Olson, T. Y.; Talley, C. E.; Zhang, J. Z. *J. Phys. Chem. B* **2006**, *110*, 19935–19944.
- (40) Mahmoud, M. A.; El-Sayed, M. A. *Nano Lett.* **2009**, *9*, 3025–3031.
- (41) Tao, A.; Kim, F.; Hess, C.; Goldberger, J.; He, R. R.; Sun, Y. G.; Xia, Y. N.; Yang, P. D. *Nano Lett.* **2003**, *3*, 1229–1233.
- (42) Zhang, J.; Langille, M. R.; Mirkin, C. A. *Nano Lett.* **2011**, *11*, 2495–2498.
- (43) Nehl, C. L.; Liao, H. W.; Hafner, J. H. *Nano Lett.* **2006**, *6*, 683–688.
- (44) Mahmoud, M. A.; Snyder, B.; El-Sayed, M. A. *J. Phys. Chem. C* **2010**, *114*, 7436–7443.
- (45) Kelly, K. L.; Coronado, E.; Zhao, L. L.; Schatz, G. C. *J. Phys. Chem. B* **2003**, *107*, 668–677.
- (46) Caruso, F.; Caruso, R. A.; Mohwald, H. *Science* **1998**, *282*, 1111–1114.
- (47) Yin, Y. D.; Rioux, R. M.; Erdonmez, C. K.; Hughes, S.; Somorjai, G. A.; Alivisatos, A. P. *Science* **2004**, *304*, 711–714.
- (48) Narayanan, R.; El-Sayed, M. A. *Nano Lett.* **2004**, *4*, 1343–1348.
- (49) Zeng, J.; Zhang, Q.; Chen, J. Y.; Xia, Y. N. *Nano Lett.* **2010**, *10*, 30–35.
- (50) Mahmoud, M. A.; Saira, F.; El-Sayed, M. A. *Nano Lett.* **2010**, *10*, 3764–3769.
- (51) Mahmoud, M. A.; El-Sayed, M. A. *Nano Lett.* **2011**, *11*, 946–953.
- (52) Macdonald, J. E.; Bar Sadan, M.; Houben, L.; Popov, I.; Banin, U. *Nat. Mater.* **2010**, *9*, 810–815.
- (53) Yen, C. W.; Mahmoud, M. A.; El-Sayed, M. A. *J. Phys. Chem. A* **2009**, *113*, 4340–4345.
- (54) Snyder, J.; McCue, I.; Livi, K.; Erlebach, J. J. *Am. Chem. Soc.* **2012**, *134*, 8633–8645.
- (55) Yadav, M.; Akita, T.; Tsumori, N.; Xu, Q. *J. Mater. Chem.* **2012**, *22*, 12582–12586.
- (56) Hong, J. W.; Kang, S. W.; Choi, B. S.; Kim, D.; Lee, S. B.; Han, S. W. *ACS Nano* **2012**, *6*, 2410–2419.
- (57) Eddoudi, M.; Kim, J.; Rosi, N.; Vodak, D.; Wachter, J.; O’Keeffe, M.; Yaghi, O. M. *Science* **2002**, *295*, 469–472.
- (58) Graessner, M.; Pippel, E.; Greiner, A.; Wendorff, J. H. *Macromolecules* **2007**, *40*, 6032–6039.
- (59) Park, J. C.; Bang, J. U.; Lee, J.; Ko, C. H.; Song, H. J. *Mater. Chem.* **2010**, *20*, 1239–1246.
- (60) Mahmoud, M. A.; Narayanan, R.; El-Sayed, M. A. *Acc. Chem. Res.* **2013**, *46*, 1795–1805.
- (61) Faraday, M. *Philos. Trans. R. Soc. London* **1847**, *147*, 145–158.
- (62) Zsigmondy, R. *The Chemistry of Colloids*; John Wiley & Sons, Inc.: New York, 1917.
- (63) Millstone, J. E.; Hurst, S. J.; Metraux, G. S.; Cutler, J. I.; Mirkin, C. A. *Small* **2009**, *5*, 646–664.
- (64) Wang, Z. L.; Kang, Z. C. *Functional and Smart Materials: Structure Evaluation and Structure Analysis*; Plenum: New York, 1998; Chapter 6.
- (65) Wiley, B.; Sun, Y. G.; Mayers, B.; Xia, Y. N. *Chem.—Eur. J.* **2005**, *11*, 454–463.
- (66) Xia, X. H.; Xia, Y. N. *Nano Lett.* **2012**, *12*, 6038–6042.
- (67) Wiley, B.; Herricks, T.; Sun, Y. G.; Xia, Y. N. *Nano Lett.* **2004**, *4*, 1733–1739.
- (68) Fan, H. J.; Knez, M.; Scholz, R.; Hesse, D.; Nielsch, K.; Zacharias, M.; Gosele, U. *Nano Lett.* **2007**, *7*, 993–997.
- (69) Berger, S. D.; Gibson, J. M.; Camarda, R. M.; Farrow, R. C.; Huggins, H. A.; Kraus, J. S.; Liddle, J. A. *J. Vac. Sci. Technol. B* **1991**, *9*, 2996–2999.
- (70) Haynes, C. L.; Van Duyne, R. P. *J. Phys. Chem. B* **2001**, *105*, 5599–5611.
- (71) Lee, J. H.; Mahmoud, M. A.; Sitterle, V.; Sitterle, J.; Meredith, J. C. *J. Am. Chem. Soc.* **2009**, *131*, 5048–5049.
- (72) Lee, J. H.; Mahmoud, M. A.; Sitterle, V. B.; Sitterle, J. J.; Meredith, J. C. *Chem. Mater.* **2009**, *21*, 5654–5663.
- (73) Mahmoud, M. A.; Snyder, B.; El-Sayed, M. A. *J. Phys. Chem. Lett.* **2010**, *1*, 28–31.
- (74) Mahmoud, M. A.; El-Sayed, M. A. *J. Phys. Chem. C* **2008**, *112*, 14618–14625.
- (75) Creighton, J. A.; Blatchford, C. G.; Albrecht, M. G. *J. Chem. Soc., Faraday Trans. 2* **1979**, *75*, 790–798.
- (76) Jeanmaire, D. L.; Van Duyne, R. P. *J. Electroanal. Chem. Interfacial Electrochem.* **1977**, *84*, 1–20.
- (77) Otto, A.; Timper, J.; Billmann, J.; Kovacs, G.; Pockrand, I. *Surf. Sci.* **1980**, *92*, 55–57.
- (78) Moskovits, M. *Rev. Mod. Phys.* **1985**, *57*, 783.
- (79) Mahmoud, M. A.; Tabor, C. E.; El-Sayed, M. A. *J. Phys. Chem. C* **2009**, *113*, 5493–5501.
- (80) Chen, H.; Kou, X.; Yang, Z.; Ni, W.; Wang, J. *Langmuir* **2008**, *24*, 5233–5237.
- (81) Khalavka, Y.; Becker, J.; Soennichsen, C. *J. Am. Chem. Soc.* **2009**, *131*, 1871–1875.
- (82) Mahmoud, M. A.; Chamanza, M.; Adibi, A.; El-Sayed, M. A. *J. Am. Chem. Soc.* **2012**, *134*, 6434–6442.
- (83) Sun, Y.; Xia, Y. *Anal. Chem.* **2002**, *74*, 5297–5305.
- (84) Mahmoud, M. A.; El-Sayed, M. A. *J. Am. Chem. Soc.* **2010**, *132*, 12704–12710.
- (85) Mahmoud, M. A.; El-Sayed, M. A. *J. Phys. Chem. B* **2013**, *117*, 4468–4477.
- (86) Mahmoud, M. A.; Chamanzar, M.; Adibi, A.; El-Sayed, M. A. *J. Am. Chem. Soc.* **2012**, *134*, 6434–6442.

- (87) Bohren, C. F. *Absorption and Scattering of Light by Small Particles*; Wiley Interscience Publication: New York, 1983.
- (88) Mahmoud, M. A.; El-Sayed, M. A. *Langmuir* **2012**, *28*, 4051–4059.
- (89) Weng, G.; Mahmoud, M. A.; El-Sayed, M. A. *J. Phys. Chem. C* **2012**, *116*, 24171–24176.
- (90) Mahmoud, M. A.; Weng, G. *Catal. Commun.* **2013**, *38*, 63–66.
- (91) Mahmoud, M. A.; Szymanski, P.; El-Sayed, M. A. *J. Phys. Chem. Lett.* **2012**, *3*, 3527–3531.
- (92) Link, S.; El-Sayed, M. A. *Annu. Rev. Phys. Chem.* **2003**, *54*, 331–366.
- (93) Hartland, G. V. *Chem. Rev.* **2011**, *111*, 3858–3887.
- (94) Del Fatti, N.; Voisin, C.; Chevy, F.; Vallee, F.; Flytzanis, C. *J. Chem. Phys.* **1999**, *110*, 11484–11487.
- (95) Hodak, J. H.; Martini, I. *J. Chem. Phys.* **1998**, *108*, 9210–9213.